Predictability and randomization of surface air temperature chaotic dynamics

Alexander Bershadskii
ICAR, P.O. Box 31155, Jerusalem, Israel, 91000

Abstract
The surface air temperature daily records at the land-based locations with different climate conditions (from the Arctic to Patagonia) have been studied on the daily to intraseasonal time scales (low-frequency annual and seasonal variations have been removed by subtracting a wavelet regression from the daily records). It is shown that the power spectra of the daily time series exhibit a universal behavior corresponding to distributed chaos dominated by the buoyancy-inertial and buoyancy-diffusive mechanisms. Global average temperature fluctuations (land-based data) and the tropical Pacific sea surface temperature fluctuations (El Niño/La Niña phenomenon) have also been considered in this context. It is shown that the practical smooth predictability for the surface air temperature dynamics is possible at least up to the fundamental (pumping) period of the distributed chaos.

Keywords Atmospheric surface layer · predictability · chaos · buoyancy-driven convection

A. Bershadskii
E-mail: bershads@gmail.com

1 Introduction

The digital databases with numerous long-term local meteorological records open new possibilities for a comparative analysis of the meteorological data over areas with different climate conditions (Baranowski et al. 2015). This analysis is crucial for understanding of the differences and universal properties in the dynamics of the meteorological processes. The (near) surface temperature is one of the most significant meteorological characteristics. Due to dependence on many different factors (such as latitude, elevation, atmospheric and oceanic circulations, coastal or interior location, terrain, etc.) the land-based (near) surface air temperature is not expected to possess universal properties, especially on the daily to intraseasonal time scales. On the other hand, the chaotic nature of the temperature dynamics at these time scales can result in some universality (see, for instance, Slingo and Palmer 2011). In the present paper, we will try to find out these universal features, which appear to be rather strong. Of course, a comprehensive analysis of this universality on global scales is far beyond of our present scope. But already a preliminary glance at some geographical locations scattered around the globe reveals a rather interesting picture, that can justify a more comprehensive analysis. These locations were chosen mostly because of the existence of sufficiently long and continuous daily records of the (near) surface temperature and a minimization of the urban effect.

There is another approach: a large-scale space average of the local temperature fluctuations. This approach can provide a global average temperature daily time series (see, for instance, Rohde et al. 2013; Berkeley Earth 2025 and references therein). An analysis of these time series can then be compared with the analysis of the space-localized data.

Daily data for the surface air temperature over oceans as well as for the sea surface temperature - SST (i.e., the water temperature near the ocean's surface) are, naturally, much less available for a sufficiently long period. However, for the most interesting area of the Pacific Ocean (its tropical part) the data have been accumulated in relation to the important El Niño/La Niña phenomenon. This phenomenon affects the surface air temperature across the globe and it is interesting to compare its chaotic properties with those of the surface air temperature over land.

Analysis of the above-discussed data is crucial for the important problem of weather forecasting. Ideally, the predictability horizon can be extended indefinitely by reducing the initial errors. It is a smooth dynamical predictability. The smooth dynamical systems are generally characterized by the stretched exponential spectra:

$$E(f) \propto \exp -(f/f_0)^{\beta} \tag{1}$$

where f is the frequency.

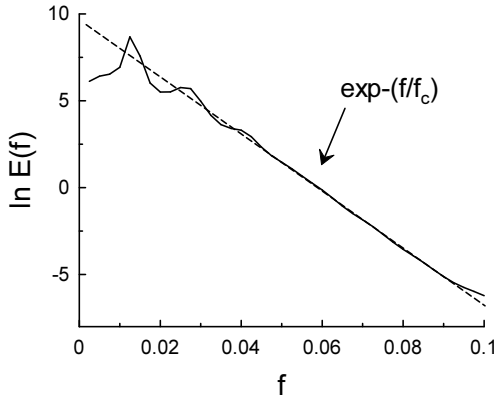

Fig. 1 Logarithm of power spectrum for z-component of the Eq. (3) against frequency f. The dashed straight line corresponds to Eq. (2).

For deterministic chaos $\beta = 1$ (Ohtomo et al. 1995)

$$E(f) \propto \exp -(f/f_c) \tag{2}$$

The seminal Lorenz system is a very simplified (on the first Galerkin modes) model for Rayleigh-Bénard (thermal) convection in a layer of fluid, cooled from above and heated from below:

$$\frac{dx}{dt} = \sigma(y - x), \quad \frac{dy}{dt} = rx - y - xz, \quad \frac{dz}{dt} = xy - bz \tag{3}$$

The parameters $b = 8/3$, $r = 28.0$, $\sigma = 10.0$ provide a chaotic solution Ecke (2015). Fig. 1 shows the power spectrum of z-component (in the semi-logarithmic scales). The spectrum was computed using the maximum entropy method, which provides an optimal resolution for comparatively short data sets Ohtomo et al. (1995). The dashed straight line corresponds to Eq. (2) in the semi-logarithmic scales.

For $1 > \beta$, the chaotic dynamics is smooth but randomized (not deterministic) (Wu et al. 1990). This chaotic dynamics will be called distributed chaos (see below for clarification of the term). The non-smooth dynamics (hard turbulence according to Wu et al. 1990) is characterized by the power-law (scaling) spectra. The value of the parameter β can be used as a measure of the randomization: the further the value of β is from $\beta = 1$, the stronger is randomization.

In reality forecasting window is always restricted by a frequency range where the spectrum can be approximated by the stretched exponential Eq. (1)

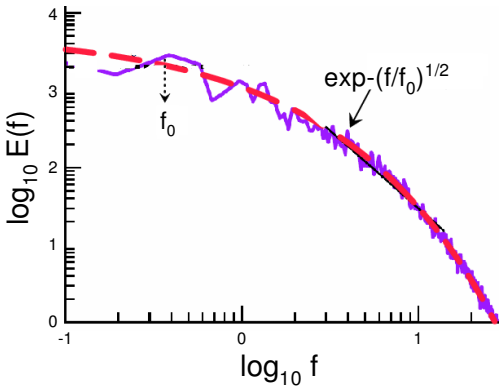

Fig. 2 Power spectrum (in the log-log scales) of the temporal temperature fluctuations in the center of a cube for a direct numerical simulation of the Rayleigh-Bénard convection.

(see, for instance, Bershadskii 2025 and below).

Figure 2 shows a frequency power spectrum for the temporal temperature fluctuations obtained in direct numerical simulations (DNS) of the buoyancy driven convection under Boussinesq approximation

$$\frac{\partial \mathbf{u}}{\partial t} + (\mathbf{u}\cdot\nabla)\mathbf{u} = -\frac{\nabla p}{\rho_0} + \sigma g\theta \mathbf{e}_z + \nu\nabla^2\mathbf{u} \tag{4}$$

$$\frac{\partial \theta}{\partial t} + (\mathbf{u}\cdot\nabla)\theta = S\frac{\Delta}{H}e_z u_z + \kappa\nabla^2\theta, \tag{5}$$

$$\nabla\cdot\mathbf{u} = \mathbf{0} \tag{6}$$

where θ is the temperature fluctuations over a temperature profile $T_0(z)$, p is the pressure, $\mathbf{u}$ is the velocity, $\mathbf{e}_z$ is a unit vector along the gravity direction, g is the gravity acceleration, H is the distance between the layers and Δ is the temperature difference between the layers, ρ_0 is the mean density, ν is the viscosity and κ is the thermal diffusivity, σ is the thermal expansion coefficient. For the unstable stratification $S = +1$ and for the stable stratification $S = -1$.

The equations were numerically solved with conducting boundary conditions for the temperature field at the horizontal walls (heating from below and cooling from above) and insulating boundary conditions at the side walls. The no-slip boundary conditions were used at all the walls for the velocity field. The DNS was performed for the Prandtl number $Pr = 1$ and Rayleigh number $Ra = 10^8$.

The spectral data for Fig. 2 were taken from Fig. 7 of the Ref. (Kumar and Verma 2018). The measurements in these DNS were made with the real-space probes located at the centre of a box. The mean velocity at the centre of the

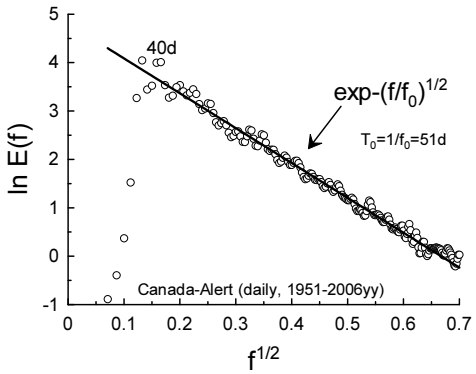

Fig. 3 The power spectrum of the daily mean surface air temperature measured at Alert location (Nunavut, Canada).

cubical box has a zero value. Therefore, the measurements provide a real temporal (frequency) spectrum (Kumar and Verma 2018).

The dashed curve in Fig. 2 indicates the stretched exponential spectrum Eq. (1) with $\beta = 1/2$, and the dotted vertical arrow indicates the location of the frequency f_0. From the location of f_0 (the maximum of $E(f)$) one can see that the entire distributed chaos is tuned to the low-frequency coherent structures in this case.

The stretched exponential form of the power spectrum indicates the smooth predictability for this numerical simulation despite a considerable randomization ($\beta = 1/2$).

2 Distributed chaos in the buoyancy-driven flows

2.1 Buoyancy-inertial mechanism

Equations (4-6) at $\nu = \kappa = 0$ and vanishing or periodic boundary conditions have an invariant - a generalized energy:

$$\mathcal{E} = \int_V (\mathbf{u}^2 - S\sigma g \frac{H}{\Delta}\theta^2)\, d\mathbf{r} \tag{7}$$

where V is the spatial volume (see, for instance, Kumar et al. (2014)). It can be readily shown that the presence of a global rotation does not change the

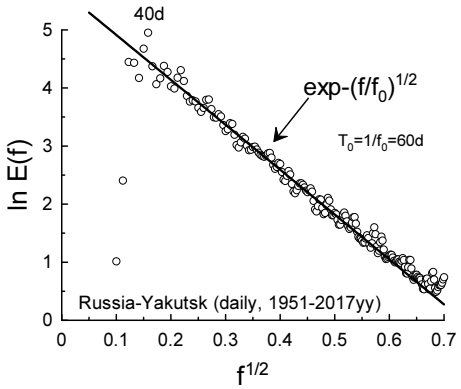

Fig. 4 The power spectrum of the daily mean surface air temperature measured at Yakutsk (Russia, Siberia).

invariant Eq. (7).

Taking into account phenomenological ideas of Kolmogorov, Bolgiano and Obukhov (Monin and Yaglom 2007), we can obtain (using the dimensional considerations) a relationship between characteristic temperature fluctuations θ_c and the characteristic frequency scale f_c

$$\theta_c \propto (\sigma g)^{-1} \varepsilon^{1/2} f_c^{1/2}, \tag{8}$$

where the generalized dissipation/transfer rate

$$\varepsilon = \left| \frac{d\langle \mathbf{u}^2 - S\sigma g \frac{d}{\Delta} \theta^2 \rangle}{dt} \right| \tag{9}$$

$\langle ... \rangle$ denotes spatial averaging.

To take into account the possibility of random fluctuations of f_c (together with θ_c, Eq. (8)), one should consider an ensemble average of the exponential spectra Eq. (2) (deterministic chaos)

$$E(f) = \int P(f_c) \ \exp -(f/f_c) \ df_c. \tag{10}$$

This approach determines the distributed chaos as a smooth randomization of the deterministic one.

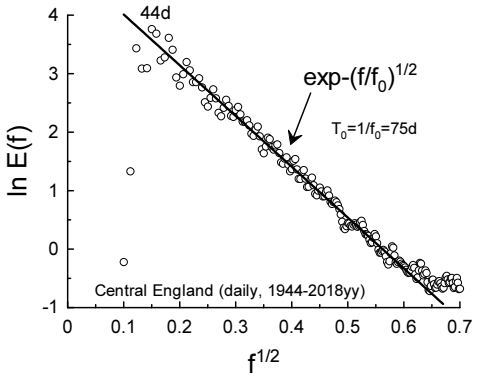

Fig. 5 The power spectrum of the daily mean surface air temperature measured at Central England for the period 1944-2018yy.

If the characteristic temperature fluctuations θ_c are half-normally distributed: $P(\theta_c) \propto \exp -(\theta_c^2/2\sigma_c^2)$, then the probability distribution $P(f_c)$ can be readily calculated using Eq. (8)

$$P(f_c) \propto f_c^{-1/2} \exp -(f_c/4f_0) \tag{11}$$

where f_0 is a renormalized (due to the fluctuations) characteristic frequency.

Substituting Eq. (11) into Eq. (10) we obtain

$$E(f) \propto \exp -(f/f_\beta)^{1/2} \tag{12}$$

i.e., the distributed chaos with $\beta = 1/2$ (cf Fig. 2).

2.2 **Buoyancy-diffusive mechanism**

As mentioned in the previous subsection 2.1, the invariance of the generalized energy $\mathcal{E}$ is conditioned by the applicability of certain boundary conditions. If the boundary conditions are not favorable for the invariance of the generalized energy, then the parameter ε in the estimate Eq. (8) can be replaced by another, wildly used for the turbulent flows, phenomenological integral parameter – eddy diffusivity of heat K_h (see, for instance, Li et al. 2015 and references therein). In this case we obtain from the dimensional considerations

$$\theta_c \propto (\sigma g)^{-1} K_h^{1/2} f_c^{3/2} \tag{13}$$

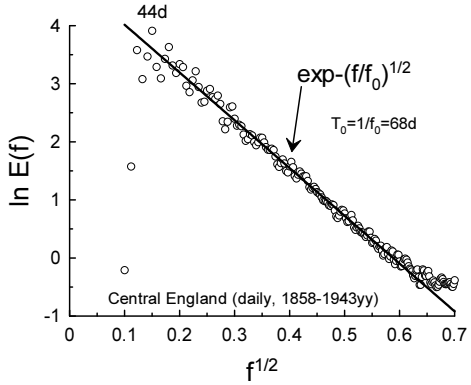

Fig. 6 As in Fig. 5 but for the historical period 1858-1943yy.

It is a more complex task to find the spectrum $E(f)$ for this case. Let us rewrite Eq. (10) in the form

$$E(f) \propto \int_0^\infty P(f_c) \exp -(f/f_c)\ df_c \propto \exp -(f/f_0)^\beta \tag{14}$$

The Eq. (14) can be used to estimate $P(f_c)$ for large f_c (Johnston 2006)

$$P(f_c) \propto f_c^{-1+\beta/[2(1-\beta)]}\ \exp(-\gamma f_c^{\beta/(1-\beta)}) \tag{15}$$

Let us generalize equations (8) and (13) as

$$\theta_c \propto f_c^\alpha \tag{16}$$

In the case of half-normally distributed positive variable θ_c, a relationship between the exponents β and α can be obtained from Eqs. (15) and (16) (using some algebra)

$$\beta = \frac{2\alpha}{1+2\alpha} \tag{17}$$

It follows from Eq. (17) that for $\alpha = 3/2$ (Eq. (13)) the parameter $\beta = 3/4$, i.e. the spectrum in this case has the form

$$E(f) \propto \exp -(f/f_0)^{3/4} \tag{18}$$

3 Northern Hemisphere

The power spectra of the local surface air temperature fluctuations at 11 different geographical locations around the globe are shown in Figs. 3-14. The spectra have been computed using the maximum entropy method with an optimal resolution (Ohtomo et al. 1995). Low-frequency annual and seasonal variations have been removed by subtracting a wavelet (symmlet of order four) regression from the daily time series (Ogden 1997). This subtraction also removes the long-term trends, and the remaining time series represent the daily to intraseasonal dynamics only (cf. Wheeler and Hendon 2004; Ventrice et al. 2013).

Let us start from the Alert (Qikiqtaaluk Region, Nunavut, Canada) - the northernmost permanently inhabited location on the globe, far north of the Arctic Circle (Latitude: 82.5018 and Longitude: -62.3481, elevation: 30 m). The climate is of a very dry polar type. Figure 3 shows the power spectrum of the daily mean surface air temperature measured for the 1951–2006yy (the data were taken from the site Climate 2025). The straight line in the figure (the best fit) indicates, in the appropriately chosen scales, the stretched exponential decay Eq. (12) with the $\beta = 1/2$. The fundamental (pumping) period $T_f \simeq 40$d.

Yakutsk (Russia, Sakha Republic, Siberia) - located 450 kilometers south of the Arctic Circle (Latitude: 62.0354 and Longitude: 129.6755, elevation: 126 m). Yakutsk has an extreme subarctic climate with a distinct inland location. The winters are extremely long and cold (the lowest temperature recorded here -64.4 ^{0}C), while summers are warm (daily max. temperatures can exceed +30 $^{\circ 0}$C). The climate is rather dry. Figure 4 shows the power spectrum of the daily mean surface air temperature measured for the 1951–2017yy (the data were taken from the site Aisori 2025). The straight line in the figure (the best fit) indicates, in the appropriately chosen scales, the stretched exponential decay Eq. (12) with the $\beta = 1/2$. The fundamental (pumping) period $T_f \simeq 40$d.

Next, let us look at Central England with its temperate maritime climate. Although the urban effect is rather considerable at this region (a triangular area enclosed by London, Bristol, and Lancashire - Latitude: 53.7632, Longitude: -2.7044) there is a long continuous data set of the mean daily temperatures (Hadcet 2025; Parker 1992) that allows to compare the temperature power spectra for a modern (the 1944-2018yy) and an historical (1858–1943yy) periods (see Figs. 5 and 6). And again the both decaying parts of the spectra correspond to the stretched exponential Eq. (12) with the same $\beta = 1/2$. The fundamental (pumping) period in both these cases: $T_f \simeq 44$d, is also close to that observed in the previous cases.

Next is the Balkhash city (Kazakhstan, Central Asia - Latitude: 46.8435, Longitude: 74.9810, elevation: 440 m) with its semi-arid (continental) climate.

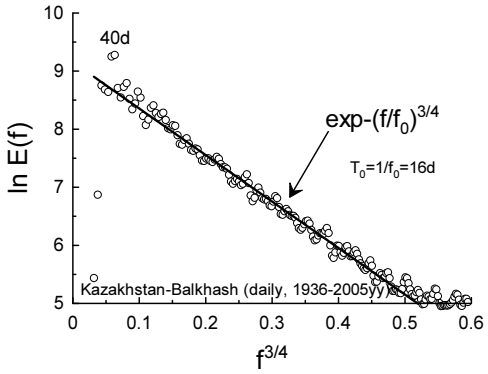

Fig. 7 The power spectrum of the daily mean surface air temperature measured at Balkhash (Kazakhstan, Central Asia).

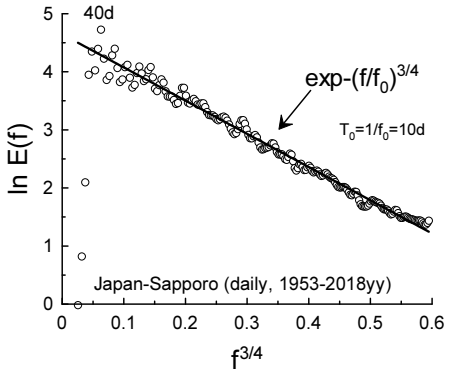

Fig. 8 The power spectrum of the daily mean surface air temperature measured at Sapporo (Japan).

Although the city is located on the northern shore of Lake Balkhash (one of the largest lakes in Asia), precipitation is low. Figure 7 shows the power spectrum of the daily mean surface air temperature measured for the 1936–2005yy (the data were taken from the site Ecad 2025). The straight line in the figure (the best fit) indicates, in the appropriately chosen scales, the stretched exponential decay Eq. (18) now with the $\beta = 3/4$. The fundamental (pumping) period $T_f \simeq 40$d.

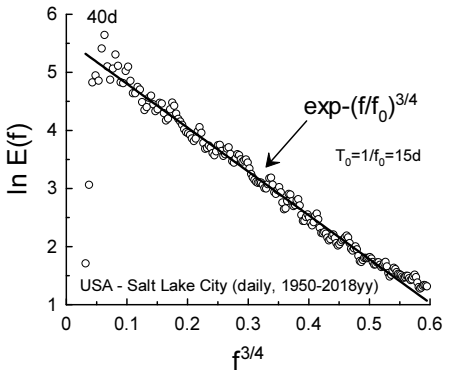

Fig. 9 The power spectrum of the daily mean surface air temperature measured at Salt Lake City (Utah, USA).

Sapporo (Japan, Latitude: 43.0625, Longitude: 141.3536, elevation: 26 m) has a humid continental climate with significant rainfall. Figure 8 shows the power spectrum of the daily mean surface air temperature measured for the 1953–2018yy (the data were taken from the site NOAA 2025). The straight line in the figure (the best fit) indicates, in the appropriately chosen scales, the stretched exponential decay Eq. (18) with the $\beta = 3/4$ (cf. Fig. 7). The fundamental (pumping) period $T_f \simeq 40$d.

As the Sapporo the Salt Lake City (Utah, USA - Latitude: 40.7608, Longitude: -111.8910, elevation 1304 m) has a hot-summer humid continental climate. The Pacific Ocean and the Great Salt Lake are considered the primary influences on the weather of this location. Figure 9 shows the power spectrum of the daily mean surface air temperature measured for the 1950–2018yy (the data were taken from the site NOAA 2025). The straight line in the figure (the best fit) indicates the stretched exponential decay Eq. (18) with the $\beta = 3/4$ (cf. Figs. 7 and 8). The fundamental (pumping) period $T_f \simeq 40$d.

4 Tropics

Now let us jump to the tropics - Darwin (in the top end of Northern Australia, Latitude: -12.4634, Longitude: 130.8456, elevation: 37 m). It has a tropical savanna climate, that is characterized by very stable mean daily temperature all year round, with clear distinct dry and wet seasons. The wet season is characterised by monsoonal rains and high humidity, while the dry season is

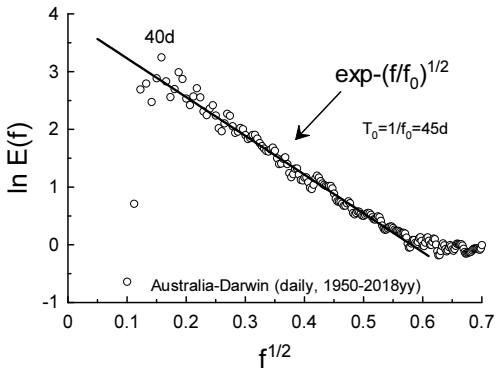

Fig. 10 The power spectrum of the daily mean surface air temperature measured at Darwin (Northern Australia).

characterised by cool nights and sunny warm days. Figure 10 shows the power spectrum of the daily mean surface air temperature measured for the 1950–2018yy (the data were taken from the site NOAA 2025). The straight line in the figure (the best fit) indicates the stretched exponential decay Eq. (12) with the $\beta = 1/2$. The fundamental (pumping) period $T_f \simeq 40$d. The power spectrum is rather similar to those observed at the high latitudes (cf. Figs. 3-6).

5 Southern Hemisphere

Dissimilarity between the Northern and Southern hemispheres' geographic setting in respect of the land-ocean distribution could result in significant differences in the time variability of the surface air temperature. However, as it will be seen from the figures 11-14, the main properties of the above-discussed distributed chaos at the daily to intraseasonal time scales are also valid for the Southern Hemisphere. Only the values of the fundamental (pumping) period are different.

Alice Springs (central Australia, Latitude: -23.6980, Longitude: 133.8807, elevation: 545 m) has a desert (a semi-arid) climate with little rainfall throughout the year, hot summers, and cold winters. Figure 11 shows the power spectrum of the daily mean surface air temperature measured for the 1973–2018yy (the data were taken from the site NOAA 2025). The straight line in the figure (the best fit) indicates the stretched exponential decay Eq. (18) with the $\beta = 3/4$. The fundamental (pumping) period $T_f \simeq 33$d (cf. Figs. 7-9).

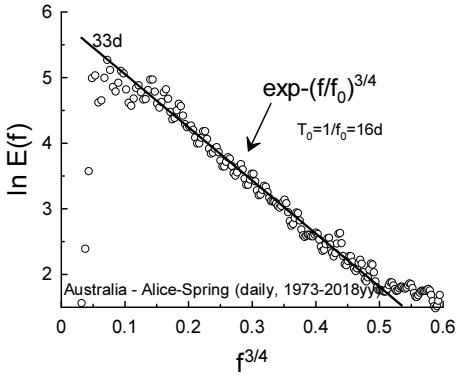

Fig. 11 The power spectrum of the daily mean surface air temperature measured at Alice Springs (Central Australia).

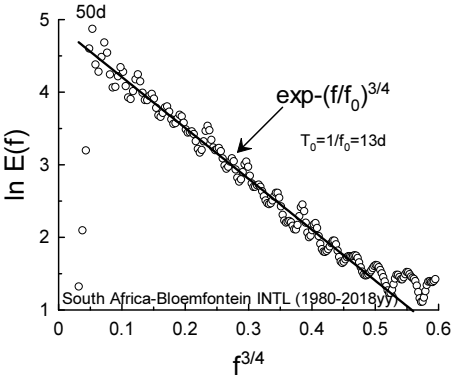

Fig. 12 The power spectrum of the daily mean surface air temperature measured at Bloemfontein (central South Africa).

The Bloemfontein (central South Africa, Latitude: -29.0852, Longitude: 26.1596, elevation: 1395 m) has a semi-arid climate with hot summers and dry, cooler winters. Figure 12 shows the power spectrum of the daily mean surface air temperature measured for the 1980–2018yy (the data were taken from the site NOAA 2025). The straight line in the figure (the best fit) indicates the stretched exponential decay Eq. (18) with the $\beta = 3/4$. The fundamental (pumping) period $T_f \simeq 50$d, that can be a consequence of the Madden-Julian

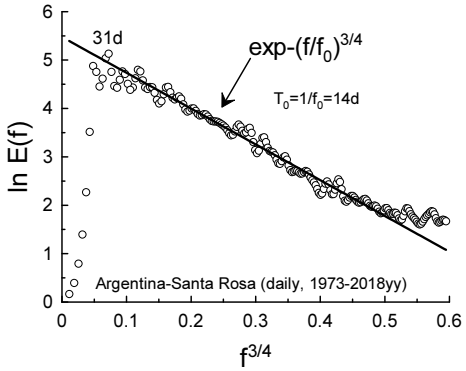

Fig. 13 The power spectrum of the daily mean surface air temperature measured at Santa Rosa (central Argentina).

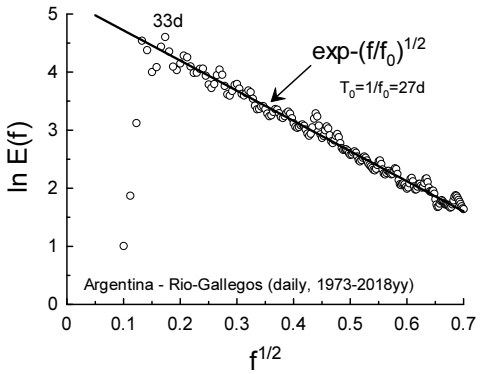

Fig. 14 The power spectrum of the daily mean surface air temperature measured at Rio Gallegos (Patagonia, Argentina).

Oscillation (Wheeler and Hendon 2004; Ventrice et al. 2013).

The Santa Rosa (central Argentina, Latitude: -36.6209, Longitude: -64.2912369, elevation: 175 m) has a humid subtropical climate with hot (warm) summers and dry, chilly winters. Figure 13 shows the power spectrum of the daily mean surface air temperature measured for 1973–2018yy (the data were taken from the site NOAA 2025). The straight line in the figure (the best fit) indicates

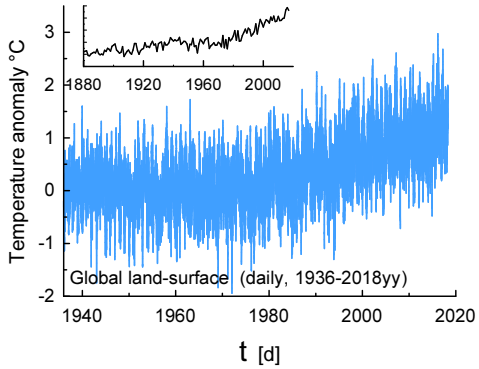

Fig. 15 Global average surface temperature anomaly for 1936-2018yy. The land-based daily data were taken from the Ref. (Berkeley Earth 2025). The insert shows the annual mean of the surface temperature anomaly (land-based) for 1880-2017yy.

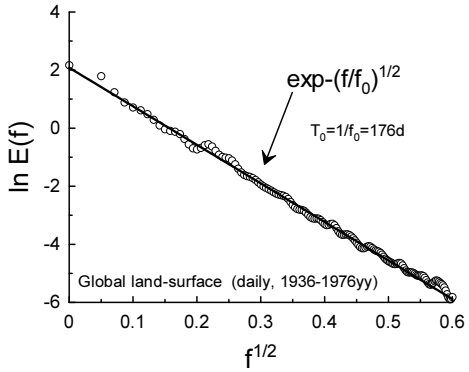

Fig. 16 Power spectrum corresponding to the sub-set (1936-1976yy) of the daily data shown in Fig. 15.

the stretched exponential decay Eq. (18) with the $\beta = 3/4$. The fundamental (pumping) period $T_f \simeq 31$d (cf. Figs. 11 and 12).

The Rio Gallegos (Patagonia, Argentina, Latitude: -51.6230, Longitude: -69.2168, elevation: 20 m) has a cold semi-arid climate (with low precipitation and very strong winds). Figure 14 shows the power spectrum of the daily

mean surface air temperature measured for the 1973–2018yy (the data were taken from the site NOAA 2025). The straight line in the figure indicates the stretched exponential decay Eq. (12) with the $\beta = 1/2$. The fundamental (pumping) period $T_f \simeq 33$d.

6 Global temperature

Figure 15 shows a global average surface temperature anomaly (relative to the Jan. 1951 - Dec. 1980 average). The land-based daily data for the 1936-2018yy were taken from the site (Berkeley Earth 2025). The entire daily time series shown in Fig. 15 is statistically non-stationary, and a certain detrending is necessary before a spectral analysis. But before the detrending, it should be noted that the time sub-series for the 1936–1976yy is approximately statistically stationary, and the spectral computation can be performed for this sub-series without detrending. Figure 16 shows the power spectrum corresponding to this statistically stationary subset of the data. The straight line in the figure (the best fit) indicates the stretched exponential decay Eq. (12) with the $\beta = 1/2$.

The second part of the time series, for the 1977–2018yy, can be detrended using the simplest linear regression method. Figure 17 shows the corresponding power spectrum. The straight line in the figure (the best fit) indicates the stretched exponential decay Eq. (12) with the $\beta = 1/2$.

On can conclude that the daily global average temperature fluctuations are dominated by the distributed chaos with $\beta = 1/2$ (the buoyancy-inertial mechanism Eq. (12)).

Interestingly, T_0 period is nearly a half-year in this case (see Figs. 16 and 17). The global temperature fluctuations can be sensitive to this period due to dissimilarity between the Northern and Southern hemispheres' geographic setting concerning the land-ocean distribution. There is also more of a difference in solar radiation between winter and summer in the Southern hemisphere than in the Northern hemisphere due to the Earth's orbit eccentricity. The northward cross-equatorial ocean heat transport plays its role as well (Kang et al. 2015).

Now let us make a detrending, removing low-frequency annual and seasonal variations by subtracting a wavelet regression from the daily time series shown in Fig. 15. The symmlet wavelets were used for this purpose for the local temperature fluctuations in the previous Sections. They are a modified version of Daubechies wavelets (with increased symmetry) (Ogden 1997). A special (and simplest) case of the Daubechies wavelet is the Haar wavelet. It is especially effective for the analysis of signals with abrupt fluctuations, that is the case of the daily global temperature fluctuations. Therefore, this wavelet regression has been used for the daily time series shown in Figure 15. Figure 18 shows the power spectrum computed for the Haar wavelet detrended entire daily time series (the 1936–2018yy).

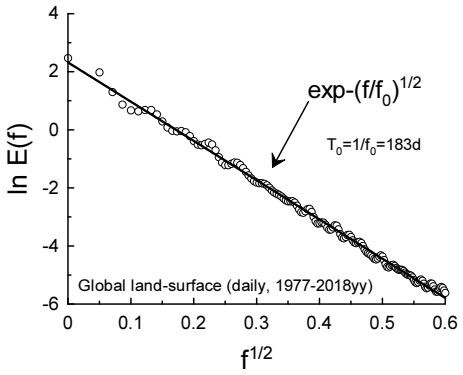

Fig. 17 Power spectrum corresponding to the sub-set (1977-2018yy) of the daily data shown in Fig. 15.

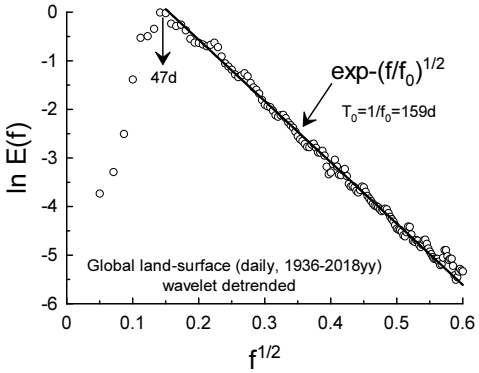

Fig. 18 Power spectrum corresponding to the wavelet regression detrended daily time series shown in Fig. 15.

The straight line in the figure (the best fit) indicates the stretched exponential decay Eq. (12) with the $\beta = 1/2$. The fundamental (pumping) period $T_f \simeq 47$d.

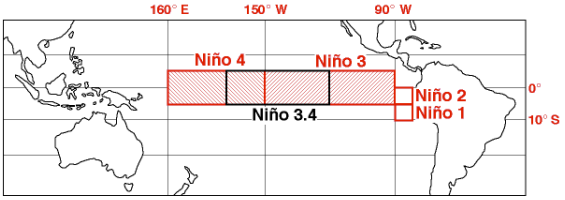

Fig. 19 Map of the tropical Pacific regions.

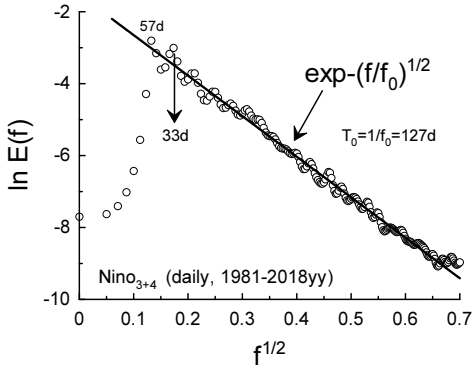

Fig. 20 Power spectrum corresponding to the wavelet regression detrended daily index Niño_{3+4} for 1981-2018yy period.

7 Tropical Pacific SST

It is well known that the El Niño/La Niña (or ENSO: El Niño - Southern Oscillation) phenomenon causes major changes in the global atmospheric circulation and, as a consequence, changes of the surface air temperatures across the globe (see, for instance, Halpert and Ropelewski 1992; Fan et al. 2017 and references therein). Therefore, it is interesting to look at the chaotic properties of this phenomenon on the daily to intraseasonal time scales and compare these properties with those of the surface air temperatures over land. The important point here is that the El Niño/La Niña indices: Niño1,...,Niño4, are the areas averaged SST (*sea* surface temperature, i.e. the water temperature near the ocean's surface). The Niño3 (5N-5S, 150W-90W region) and the Niño4 (5N-5S, 160E-150W region) indices together cover a rather wide and representative area in the tropical Pacific (see Fig. 19). In this area, the El Niño/La Niña

phenomenon is mainly observed. Figure 20 shows the power spectrum corresponding to the weighted index Niño_{3+4}, computed from the indices Niño3 and Niño4 for the entire region (5N-5S, 160E-90W), for the 1981–2018yy period. A simple weighting has been used to take into account the difference between the areas corresponding to the Nino3 and Nino4 indices. The data for computations were taken from the site (Climexp 2025) and the low-frequency annual and seasonal variations have been removed by subtracting the wavelet (symmlet of order four, used above for the local surface air temperature fluctuations) regression from the daily time series. The straight line in the figure (the best fit) indicates the stretched exponential decay Eq. (12) with the $\beta = 1/2$.

8 Predictability limitations

After the seminal paper (Lorenz 1969) the predictability problem obtained several new trends which dominate its development even now.

1. There were introduced two main types of predictability. Let us define them as the *smooth* and *rough* ones (see Introduction). At the *smooth* predictability, the predictability horizon can be indefinitely extended by reducing the initial error. At the *rough* predictability, the predictability horizon cannot be indefinitely extended by reducing the initial error. It was generally assumed that the real weather forecasts belong to the second type of predictability, with a finite horizon that cannot be larger than two weeks (approximately).

2. Following Kolmogorov's scaling paradigm (Monin and Yaglom 2007) it was assumed that the power-law spectra completely determine the real weather forecasts. Since this assumption, the power-law spectra were the main theoretical tool in this respect. There were many attempts to find such spectra for the simulations and naturally observed data (see, for instance, Sun and Zhang 2016 and references therein).

3. It was assumed that for the power-law spatial (wavenumber) spectra of the kinetic energy $E(k) \propto k^{-\gamma}$ with the $\gamma < 3$, the predictability is rough.

4. The main predictability efforts were concentrated on the space properties of the velocity field and the temperature field was considered as a secondary one for the weather predictability problem (Vannitsem et al. 2019).

Now it is clear that the stretched exponential frequency spectra Eqs. (12) and (18) can be considered as strong indicator of the smooth predictability. The first example given in the present paper - the Rayleigh-Bénard thermal convection, provides a clue to the situation. In this case, the entire frequency range covered by the distributed chaos with the stretched exponential spectrum is tuned to the fundamental (pumping) frequency f_0 (the low-frequency coherent structures). Generally, the fundamental (pumping) periods indicated in the Figs. 3-14 can be considered as practical forecast windows of the surface air temperature dynamics for these cases. It means that the practical smooth predictability of the air surface temperature dynamics is possible *at least* up to the corresponding time scales.

9 Conclusions

A. The apparent universality of the surface air temperature spectra on the daily to intraseasonal time scales can be related to the domination of the two (buoyancy-inertial and buoyancy-diffusive) mechanisms driving the surface air temperature's dynamics. Of course, the cases considered in the paper are examples only and there should be a comprehensive analysis of as numerous as possible local records of the surface air temperature to check out this universality and to find out its limitations.

B. For Central England, there is no significant difference in the universal spectrum between a Modern (1944–2018yy) and a Historical (1858–1943yy) periods (cf. Figs 5 and 6).

C. It seems that the value $\beta = 3/4$ corresponds to most of the mid-latitudes, whereas the value $\beta = 1/2$ corresponds to the high-latitudes and tropics.

D. The fundamental (pumping) period $T_f \simeq 40$ day seems to be a universal one for the Northern Hemisphere. The near-40-day oscillations at the Northern Hemisphere extratropics are well known from numerous observations and are theoretically associated with the interaction of topography with the non-zonal flows (cf. Magana 1993; Marcus 1994; Robertson, and Mechoso 2003; Cunningham and De Albuquerque 2006 and references therein).

E. The global average surface temperature fluctuations (land-based) are dominated by the buoyancy-inertial mechanism with $\beta = 1/2$. The shift of the fundamental (pumping) period T_f toward 50 days (see Fig. 18) can be related to the effect of the Madden-Julian oscillation (see, for instance, Wheeler and Hendon 2004; Ventrice et al. 2013; Madden and Julian 1994; Zhang 2005; Hoell et al. 2014; Matsueda and Takaya 2015; Henderson 2017 and references therein), but it can also be related to the large-scale spatial averaging (cf. Figs. 5 and 6).

F. The tropical Pacific SST fluctuations on the daily to intraseasonal time scales are dominated by the buoyancy-inertial mechanism with $\beta = 1/2$ (Fig. 20). The fundamental (pumping) period $T_f \simeq 57$d can be compared to the corresponding periods of the Madden-Julian oscillation (cf. Wheeler and Hendon 2004; Ventrice et al. 2013; Madden and Julian 1994; Henderson 2017). It is not surprising because the Madden-Julian oscillation is a dynamic coupling between tropical ocean deep convection and large-scale atmospheric circulation. The second peak in the spectrum shown in Fig. 20 corresponds to period $T \simeq 33$d and can be compared to the fundamental (pumping) periods characteristic to the surface air temperature in Australia and South America (cf. Figs. 11, 13, 14, and 19).

G. The practical smooth predictability for the surface air temperature dynamics is possible at least up to the fundamental (pumping) period of the distributed chaos.

10 Acknowledgement

I acknowledge use of the data provided by the Weather, climate and hazards service of the Government of Canada, the Aisori Meteo Servise (Russia), the Met Office Hadley Centre observations datasets (UK), the European Climate Assesment&Dataset, the KNMI Climate Explorer, the Berkeley Earth dataset (USA) and the National Centers for Environmental Information, NOAA (USA). I thank Y.Q. Sun and F. Zhang for sharing their data and discussions.

References

Aisori Available at: http://aisori-m.meteo.ru
Baranowski P et al. (2015) Multifractal analysis of meteorological time series to assess climate impacts. Clim Res 65:39
Berkeley Earth Available at: https://berkeleyearth.org/data/
Bershadskii A (2025) Chaotic variability of the magnetic field at Earth's surface driven by ionospheric and space plasmas. Journal of Atmospheric and Solar–Terrestrial Physics 269:106456
Climate Available at: http://climate.weather.gc.ca
Climexp Available at: https://climexp.knmi.nl/start.cgi
Cunningham ChAC, De Albuquerque Cavalcanti IF (2006) Intraseasonal modes of variability affecting the South Atlantic Convergence Zone. Int J Climatology 26:1165
Ecke RE (2015) Chaos, patterns, coherent structures, and turbulence: Reflections on nonlinear science. Chaos, 25:097605
Ecad Available at: https://www.ecad.eu/dailydata
Fan J et al. (2017) Network analysis reveals strongly localized impacts of El Niño. PNAS 114:7543
Guilyardi E et al. (2009) Understanding El Niño in ocean–atmosphere general circulation models: Progress and challenges. Bull Am Meteorol Soc 90:325
Hadcet Available at: http://hadobs.metoffice.com/hadcet
Halpert MS, Ropelewski CF (1992) Surface temperature patterns associated with the Southern Oscillation. J Clim 5:577
Henderson SA, Maloney ED, Son S-W (2017) Madden–Julian oscillation Pacific teleconnections: The impact of the basic state and MJO representation in general circulation models. J Climate 30:4567
Hoell A et al. (2014) Disruptions of El Niño–southern oscillation teleconnections by the Madden–Julian Oscillation. Geophys Res Lett 41:998
Johnston DC (2006) Phys Rev B 74:184430

Kang SM et al. (2015) Croll revisited: Why is the northern hemisphere warmer than the southern hemisphere? Climate Dynamics 44:1457

Kumar A, Verma, MK (2018) Applicability of Taylor's hypothesis in thermally driven turbulence. Royal Soc open sci 5:172152

Kumar A, Chatterjee AG, Verma MK (2014) Energy spectrum of buoyancy-driven turbulence. Phys Rev E 90:023016

Li D, Katul GG, Zilitinkevich SS (2015) Revisiting the turbulent Prandtl number in an idealized atmospheric surface layer. J Atm Sci 72:2394–2410

Lorenz EN (1969) The predictability of a flow which possesses many scales of motion. Tellus XXI(3):289

Madden RA, Julian PR Monthly (1994) Observations of the 40–50-Day Tropical Oscillation—A Review. Weather Review 122:814

Magana V (1993) The 40-and 50-day oscillations in atmospheric angular momentum at various latitudes. J Geophys Res 98:10441

Marcus SL, Ghil M, Dickey JO (1994) The extratropical 40-day oscillation in the UCLA general circulation model. Part I: Atmospheric angular momentum. J Atmos Sci 51:1431

Matsueda S, Takaya, Y (2015) The global influence of the Madden–Julian oscillation on extreme temperature events. J Climate 28:4141

Monin AS, Yaglom AM (2007) Statistical Fluid Mechanics, Vol. II: Mechanics of Turbulence (Dover Pub. NY)

NOAA Available at https://www7.ncdc.noaa.gov/CDO/cdo

Ohtomo N, Tokiwano K, Tanaka Y et. al. (1995) Exponential characteristics of power spectral densities caused by chaotic phenomena. J Phys Soc Jpn 64:1104

Ogden T (1997) Essential Wavelets for Statistical Applications and Data Analysis (Birkhauser, Basel)

Parker DE, Legg TP, Folland CK (1992) A new daily central England temperature series, 1772–1991. Int J Clim 12:317

Peel MC, Finlayson BL., McMahon TA (2007) Updated world map of the Köppen-Geiger climate classification. Hydrol Earth Syst Sci 11:1633

Philip SY, van Oldenborgh GJ (2010) Atmospheric properties of ENSO: Models versus observations. Climate Dynamics 34:1073

Robertson AW, Mechoso CR (2003) Circulation regimes and low-frequency oscillations in the South Pacific sector. Monthly Weather Review 131:1566

Rohde R et al. (2013) Berkeley Earth Temperature Averaging Process. Geoinfor Geostat An Overview 1:2.

Sagdeev RZ, Usikov DA, Zaslavsky GM (1988) Nonlinear Physics: from the Pendulum to Turbulence and Chaos (Harwood, New York)

Slingo J, Palmer T (2011) Uncertainty in weather and climate prediction. Phil Trans R Soc A 369:4751

Sun YQ, Zhang F (2016) Intrinsic versus practical limits of atmospheric predictability and the significance of the butterfly effect. J Atmos Sci 73:1419

Trenberth KE, Caron JM, Stepaniak DP, Worley S (2002) Evolution of El Niño–Southern Oscillation and global atmospheric surface temperatures. J Geophys Res 107D8:4065

Wheeler MC, Hendon HH (2004) An all-season real-time multivariate MJO index: Development of an index for monitoring and prediction. Monthly Weather Review 132:917

Wu X-Z, Kadanoff LP, Libchaber A, Sano M (1990) Frequency power spectrum of temperature fluctuations in free convection. Phys Rev Lett 64:2140–2143

Vannitsem S, Wilks DS, Messner JW Eds. (2019) Statistical Postprocessing of Ensemble Forecasts (Elsevier, NY)

Ventrice MJ et al. (2013) A modified multivariate Madden–Julian oscillation index using velocity potential. Monthly Weather Review 141:4197

Yamasaki K, Gozolchiani A, Havlin S (2008) Climate networks around the globe are significantly affected by El Nino. Phys Rev Lett 100:228501

Zhang C (2005) Madden-Julian oscillation. Rev Geophys 43:RG2003